



1 **Numerical modelling of flow and transport in Bari industrial area by means of**  
2 **rough walled parallel plate and random walk models**

3 Claudia Cherubini<sup>(1,2)</sup>, Nicola Pastore<sup>(3)</sup>, Dimitra Rapti<sup>(4)</sup>, Concetta I. Giasi<sup>(3)</sup>

4 <sup>1</sup>Department of Physics & Earth Sciences, University of Ferrara, Via Saragat 1- 44122, Ferrara (Italy)

5 <sup>2</sup>School of Civil Engineering, University of Queensland, St Lucia, Brisbane 4072, Australia;

6 <sup>3</sup>DICATECh, Department of Civil, Environmental, Building Engineering, and Chemistry, Politecnico di Bari,  
7 Bari, Italy.

8 <sup>4</sup>New Energies And environment Company (NEA ) Via Saragat 1- 44122 Ferrara (Italy)

9  
10

11 **Abstract**

12 Modelling fluid flow and solute transport dynamics in fractured karst aquifers is one of the  
13 most challenging tasks in hydrogeology.

14 The present study investigates on the hotspots of groundwater contamination in the industrial  
15 area of Modugno (Bari –Southern Italy) where the limestone aquifer has a fractured and karstic  
16 nature.

17 A rough walled parallel plate model coupled with a geostatistical analysis to infer the values of  
18 the equivalent aperture has been implemented and calibrated on the basis of piezometric data.  
19 Using the random walk theory, the steady state distribution of hypothetical contamination with  
20 the source at the hot spot has been carried out reproducing a pollution scenario which is  
21 compatible with the observed one. From an analysis of the flow and transport pattern it is  
22 possible to infer that the anticline affecting the Calcare di Bari formation in directions ENE-  
23 WSW influences the direction of flow as well as the propagation of the contaminant.

24 The results also show that the presence of nonlinear flow influences advection, in that it leads  
25 to a delay in solute transport respect to the linear flow assumption. This is due to the not constant  
26 distribution of solute according to different pathways for fractured media which is related to  
27 the flow rate.

28 **Introduction**

29 The characterization and the description of phenomena that involve fractured aquifers,  
30 especially if considered in relationship with water resource exploitation, is an important issue  
31 because fractured aquifers serve as the primary source of drinking water for many areas of the  
32 world. In fractured rock aquifers, groundwater is stored in the fractures, joints, bedding planes  
33 and cavities of the rock mass. Water availability is largely dependent on the nature of the  
34 fractures and their interconnection. Fractures enable fast pathways for fluid flow that can



35 transport contaminants. The ability of a fracture to transmit water as well as contaminants  
36 depends primarily on the size of the opening, or the fracture aperture.

37 The parallel plate model is widely used to simulate flow in a fracture due to its simplicity of  
38 idealizing a fracture. Many workers (Baker, 1955; Huitt, 1956; Snow, 1968, 1970; Gale, 1977)  
39 have used flow between smooth parallel plates as a model for flow in fractures. The solution to  
40 the Navier-Stokes equation for flow between parallel plates, known as plane Poiseuille flow,  
41 has been known to fluid mechanics since the nineteenth century.

42 Witherspoon et al. (1980) and Elliott et al. (1985) suggested that a factor should be introduced  
43 into the parallel plate theory to take account of the effects of joint surface properties.

44 Zhao and Brown (1992) carried out hydro-thermo-mechanical tests on joints in the  
45 Carnmenellis granite from Cornwall, southwest England using a geothermal rock test facility.  
46 Experimental effective normal stress-joint closure and effective normal stress-joint  
47 permeability data were fitted by a range of deformation and hydraulic models. They applied the  
48 joint condition factor (JCF) to account for deviations from the ideal condition assumed in the  
49 smooth parallel plate theory reflecting the effects of joint roughness, joint matching, joint  
50 stiffness, deposits of detritus, loading history, sample disturbance, sample size and the  
51 temperature environment.

52 Zimmermann and Bodvarsson (1996) discussed the problem of fluid flow through a rock  
53 fracture within the context of fluid mechanics. The derivation of the 'cubic law' was given as  
54 the solution to the Navier-Stokes equations for flow between smooth, parallel plates. They  
55 analysed the various geometric and kinematic conditions that are necessary in order for the  
56 Navier-Stokes equations to be replaced by the more tractable lubrication or HeleShaw equations  
57 and reviewed various analytical and numerical results pertaining to the problem of relating the  
58 effective hydraulic aperture to the statistics of the aperture distribution.

59 They found that the effective hydraulic aperture is less than the mean aperture, by a factor that  
60 depends on the ratio of the mean value of the aperture to its standard deviation. Finally, they  
61 compared the predicted hydraulic apertures to measured values for eight data sets from the  
62 literature for which aperture and conductivity data were available on the same fracture. They  
63 concluded that reasonably accurate predictions of hydraulic conductivity can be made based  
64 solely on the first two moments of the aperture distribution function, and the proportion of  
65 contact area.

66 Some researchers proposed a variable aperture model stating that it is better adapted to describe  
67 flow and transport channeling effects than a parallel plate model (Neretnieks et al., 1982;  
68 Bourke, 1987; Pyrak-Nolte, 1988; Tsang and Tsang, 1989; Tsang et al., 2001) where fracture



69 apertures can be described by normal, (Lee et al., 2003), lognormal (e.g., Keller, 1998; Keller  
70 et al., 1999), or gamma distributions (Tsang and Tsang, 1987), or a self-affine scale invariance  
71 (Plouraboue et al., 1995).

72 Neuzil and Tracy (1981) presented a model for flow in fractures where the flow is envisioned  
73 as occurring in a set of parallel plate openings with different apertures whose distribution was  
74 lognormal and used a modified Poiseuille equation.

75 They showed that the flow conformed to the cubic law and also that the maximum flow occurs  
76 through the largest apertures, thereby emphasizing that flow occurs through preferred paths.  
77 Thus in their analysis, the flow depended on the tail of the frequency distribution.

78 Tsang and Tsang, (1987) proposed a theoretical approach to interpret flow in a tight fractured  
79 medium in terms of flow through a system of statistically equivalent one-dimensional channels  
80 of variable aperture. The channels were statistically equivalent in the sense that the apertures  
81 along each flow channel are generated from the same aperture density distribution and spatial  
82 correlation length.

83 Oron and Berkowitz (1998) have examined the validity of applying the 'local cubic law' (LCL)  
84 to flow in a fracture which is bounded by impermeable rock surfaces. A two-dimensional order-  
85 of-magnitude analysis of the Navier-Stokes equations yields three conditions for the  
86 applicability of LCL flow, as a leading-order approximation in a local fracture segment with  
87 parallel or nonparallel walls. These conditions demonstrate that the 'cubic law' is valid provided  
88 that aperture is measured not on a point-by-point basis but rather as an average over a certain  
89 length.

90 Experimental work by Plouraboué et al. (2000) in self-affine rough fractures with various  
91 translations of the opposing fracture surfaces indicated that heterogeneity in the flow field  
92 caused deviations from the parallel plate model for fracture flow.

93 Some researchers often find it convenient to represent aperture fields in terms of equivalent  
94 aperture in the parallel plate model (Zheng et al., 2008).

95 Zheng et al., 2008 carried out a systematic series of hydraulic and tracer tests on three  
96 laboratory-scale fracture replicas, and calculated the cubic law, mass balance, and frictional  
97 loss apertures. They fitted an analytical solution to the one-dimensional advection-dispersion  
98 equation to each experimental breakthrough curve three times, each time applying  $v$  based on  
99 one of the three "equivalent apertures".

100 The excellent agreement between the experimental breakthrough curves and the simulated  
101 curves based on the single-parameter curve fit applying the mass balance aperture clearly



102 demonstrates that the mass balance aperture is the only equivalent aperture appropriate for  
103 describing solute transport in single variable-aperture fractures.

104 Brush and Thomson (2003) developed three-dimensional flow models to simulate fluid flow  
105 through various random synthetic rough-walled fractures created by combining random fields  
106 of aperture and the mean wall topography or midsurface, which quantifies undulation about the  
107 fracture plane.

108 The total flow rate from three-dimensional Stokes simulations were within 10% of LCL  
109 simulations with geometric corrections for all synthetic fractures. Differences between the NS  
110 and Stokes simulations clearly demonstrated that inertial forces can significantly influence the  
111 internal flow field within a fracture and the total flow rate across a fracture.

112 Klimczak et al. (2010) carried out flow simulations through fracture networks using the discrete  
113 fracture network model (DFN) where flow was modeled through fracture networks with the  
114 same spatial distribution of fractures for correlated and uncorrelated fracture length-to-aperture  
115 relationships. Results indicate that flow rates are significantly higher for correlated DFNs.  
116 Furthermore, the length-to-aperture relations lead to power-law distributions of network  
117 hydraulic conductivity which greatly influence equivalent permeability tensor values. These  
118 results confirm the importance of the correlated square root relationship of displacement to  
119 length scaling for total flow through natural opening-mode fractures and, hence, emphasize the  
120 role of these correlations for flow modeling.

121 Wang et al. (2015) developed and tested a modified LCL (MLCL) taking into account local  
122 tortuosity and roughness, and works across a low range of local Reynolds Numbers. The MLCL  
123 was based on (1) modifying the aperture field by orienting it with the flow direction and (2)  
124 correcting for local roughness changes associated with local flow expansion/contraction. In  
125 order to test the MLCL, they compared it with direct numerical simulations with the Navier-  
126 Stokes equations using real and synthetic three-dimensional rough-walled fractures, previous  
127 corrected forms of the LCL, and experimental flow tests. The MCL proved to be more accurate  
128 than previous modifications of the LCL.

129 The CTRW approach provides a versatile framework for modelling (non-Fickian) solute  
130 transport in fractured media.

131 Berkowitz et al (2001) examined a set of analytical solutions based on the continuous time  
132 random walk (CTRW) approach to analyze breakthrough data from tracer tests to account for  
133 non-Fickian (or scale-dependent) dispersion behavior that cannot be properly quantified by  
134 using the advection-dispersion equation.



135 Cortis et al. (2008) developed a macroscopic model based on the Continuous Time Random  
136 Walk (CTRW) framework, to characterize the interaction between the fractured and porous  
137 rock domains by using a probability distribution function of residence times. They presented a  
138 parametric study of how CTRW parameters evolve, describing transport as a function of the  
139 hydraulic conductivity ratio between fractured and porous domains.

140 Srinivasan et al. (2010) presented a particle-based algorithm that treats a particle trajectory as  
141 a subordinated stochastic process that is described by a set of Langevin equations, which  
142 represent a continuous time random walk (CTRW). They used convolution based particle  
143 tracking (CBPT) to increase the computational efficiency and accuracy of these particle-based  
144 simulations. The combined CTRW–CBPT approach allows to convert any particle tracking  
145 legacy code into a simulator capable of handling non-Fickian transport.

146 Dentz et al (2016) developed a general CTRW approach for transport under radial flow  
147 conditions starting from the random walk equations for the quantification of non-local solute  
148 transport induced by heterogeneous flow distributions and by mobile-immobile mass transfer  
149 processes. They observed power-law tails of the solute breakthrough for broad distributions of  
150 particle transit times and particle trapping times. The combined model displayed an  
151 intermediate regime, in which the solute breakthrough is dominated by the particle transit times  
152 in the mobile zones, and a late time regime that is governed by the distribution of particle  
153 trapping times in immobile zones.

154 The present study is aimed at analysing the scenario of groundwater contamination of the  
155 industrial area of Modugno (Bari –Southern Italy) where the limestone aquifer has a fractured  
156 and karstic nature.

157 Previous studies carried out in the same aquifer have applied different conceptual models to  
158 model fluid flow and contaminant transport.

159 Cherubini (2008) applied the discrete feature approach (Diersch, 2002) where the 3D geometry  
160 of the subsurface domain describing the matrix structure was combined by interconnected 2D  
161 and 1D discrete feature elements in two dimensions in order to simulate respectively fractures  
162 and karstic cavities in the Bari limestone aquifer. The fracture distribution was inferred from a  
163 nonparametric geostatistical analysis (Indicator Kriging) of fracture frequency data which had  
164 been derived by RQD (Priest and Hudson, 1976) data of the contaminated area of the ex  
165 Gasometer.

166 Cherubini et al. (2008) compared the flow modelling results of the previous work with those  
167 from a new hydrogeological reconstruction of the heterogeneities in the same aquifer by means



168 of multiple realizations conditioned to borehole data (RQD population), in order to obtain a  
169 three-dimensional distribution of fracture frequency, cavities and terra rossa lenses.  
170 Cherubini and Pastore (2010) applied the nested sequential indicator simulation algorithm to  
171 represent the geological architecture of the Bari limestone aquifer which provided reliable  
172 prediction of fluid flow. According to phenols transport, the presence of preferential pathways  
173 was detected.  
174 Cherubini et al. (2013) realised a 3D flow model of Bari limestone aquifer supported by a  
175 detailed local scale geologic model realised by means of Sequential indicator simulation (SIS)  
176 of lithofacies unit sequences. In this study, a lumped parameter approach was used and  
177 calibrated on the groundwater discharge and global hydraulic gradient where fluid flow in  
178 fractures was represented by the cubic law, and Darcy–Weisbach equation was used to estimate  
179 resistance term in karst network.  
180 Masciopinto et al. (2010) adopted a conceptual model consisting of a 3D parallel set of  
181 horizontal planar fractures in between rock layers, each fracture having a variable aperture  
182 generated by a stationary random field conditioned to the data derived from pumping-tracer  
183 tests. The particle tracking solution was combined with the PHREEQC-2 results to study two-  
184 dimensional laminar/non-laminar flow and reactive transport with biodegradation in each  
185 fracture of the conceptual model.  
186 Masciopinto and Palmiotta (2013) derived new equations of fracture aperture as functions of a  
187 tortuosity factor to simulate fluid flow and pollutant transport in fractured aquifers.  
188 MODFLOW/MT3DMS water velocity predictions were compared with those obtained using a  
189 specific software application which solves flow and transport problems in a 3D set of parallel  
190 fissures. The results of a pumping/tracer test carried out in a fractured limestone aquifer in Bari  
191 (Southern Italy) have been used to calibrate advective/dispersive tracer fluxes given by the  
192 applied models. Successful simulations of flow and transport in the fractured limestone aquifer  
193 were achieved by accommodating the new tortuosity factor in models whose importance lies in  
194 the possibility of switching from a discrete to a continuum model by taking into account the  
195 effective tracer velocity during flow and transport simulations in fractures.  
196 Masciopinto and Visino (2017) carried out filtration tests on a set of 16 parallel limestone slabs  
197 having a thickness of about 1 cm where rough surfaces and variable fracture apertures had been  
198 artificially created. The experimental filtration results suggest that model simulations of  
199 perturbed virus transport in fractured soils need to also consider also pulse-like sources and  
200 sinks of viruses. This behavior cannot be simulated using conventional model equations without  
201 including a new kinetic model approach.



202 The present work focuses on the investigation of the hotspots of aquifer contamination in order  
203 to infer the location of the sources.

204 A rough walled parallel plate model has been implemented and calibrated on the basis of  
205 piezometric data and has coupled a geostatistical analysis to infer the values of the equivalent  
206 aperture.

207

### 208 **Geological and hydrogeological framework**

209 It is well known that hydraulic properties and consequently fluid circulation and contaminant  
210 propagation in carbonate rocks are strongly influenced by the degree of rock fracturing and, in  
211 general, the presence of mechanical discontinuities, like faults, joints, or other tectonic elements  
212 such as syncline or anticline axes (Caine et al., 1996; Caine and Foster, 1999; Antonellini et  
213 al., 2014; Billi et al., 2003). Also, the deformation mechanisms are mainly controlled by the  
214 physico-chemical properties of rocks, which are, in turn, the result of different composition,  
215 depositional setting and diagenetic evolution (Zhang and Spiers, 2005; Rustichelli et al., 2012).  
216 From the geological point of view, the investigated area is located in the Murge Plateau  
217 corresponding to a broad antiformal structure oriented WNW- ESE and represents the bulging  
218 foreland of the Pliocene-Pleistocene Southern Apennines orogenic belt (Pieri et al., 1997;  
219 Doglioni, 1994; Foster and Evans, 1991; Korneva et al., 2014; Parise and Pascali, 2003).

220 The stratigraphy of the Murge area consists of a Variscan crystalline basement topped by 6-7  
221 km-thick Mesozoic sedimentary cover (represented by the Calcare di Bari formation) followed  
222 by relative thin and discontinuous Cenozoic and Quaternary deposits (Calcareni di Gravina  
223 formation). Figure 1 shows the simplified geological map of the area of Bari

224

#### 225 *Calcare di Bari formation (Cretaceous)*

226 The Calcare di Bari succession consists of biopeloidal and peloidal wackestones/packstones  
227 alternating with stromatolithic bindstones with frequent intercalations of dolomitic limestones  
228 and grey dolostones. The formation

229 shows a thickness of about 470 m. Most of the Calcare di Bari formation shows facies features  
230 related to peritidal environments; only the upper part suggests a relatively more distal and  
231 deeper environment belonging to an external platform setting (CARG project, 2010; Fig.1).

232 This succession appears stratified and fissured and, where it is not interested by tectonical  
233 discontinuities, it shows a subhorizontal or slightly inclined lying position. This formation is  
234 subjected to the complex and relevant karstic phenomena that, locally lead to the formation of  
235 cavities of different shapes and sizes, partially or completely filled by “terra rossa” deposits.



236 On the basis of borehole and in situ surveys, carried out by private companies it was observed  
237 that:

238 - The fracturing degree of the Calcare di Bari formation is quite variable and it is  
239 expressed by Rock Quality Designation (RQD) values that vary between 16 and 25%  
240 (maximum borehole depths: 30 m). Based on the classification system of Deere and Deere  
241 (1988) the rock mass is of ‘very poor rock quality’ (RQD <25%).

242 - Medium values of Rock Mass Rating (RMR) about 36, indicate, after Bieniawski  
243 classification (1989), very poor rock mass (class IV).

244 - In addition, profiles of the electrical resistivity (depth < 30 m) have permitted to observe  
245 the presence of very variable electric resistivity values with variations between 100 (low  
246 fracture carbonates rocks) and 1700 Ohm\*m for very fractured formations; with locally values  
247 of the order of 3-4000 Ohm\*m, in case of underground cavities.

248 - Similarly, the velocity of the seismic waves P and S has average values of the order of  
249 1300 and 800 m/s, respectively in highly fractured limestones and 2300 (P) and 1400 (S) m/s  
250 for compact formations.

251

#### 252 *Calcareni di Gravina formation (lower Pleistocene)*

253 This unit uncomfortably lies on the Calcare di Bari Fm. Its thickness varies from few meters  
254 to 20 m and its depositional environments are related to offshore setting. The lower boundary  
255 is transgressive and is locally marked by reddish residual deposits and/or by brackish silty  
256 deposits passing upward to shallow water calcarenites rich in bioclasts.

257 As regards the structural features of these deposits it is possible to observe the anticline  
258 affecting only the Cretaceous succession of the Calcare di Bari formation in directions ENE-  
259 WSW. This tectonic structure influences the direction of flow as shown in Fig. 1. Also, the  
260 presence of this fault line with direction NE-SW, controls the development of the actual  
261 hydrographic network.

262 The limestone bedrock hosts a wide and thick aquifer. The intense fracturing of the rock and  
263 the karst phenomenon result in a high permeability of the limestone where the groundwater  
264 flows primarily through the fractures and open joints.

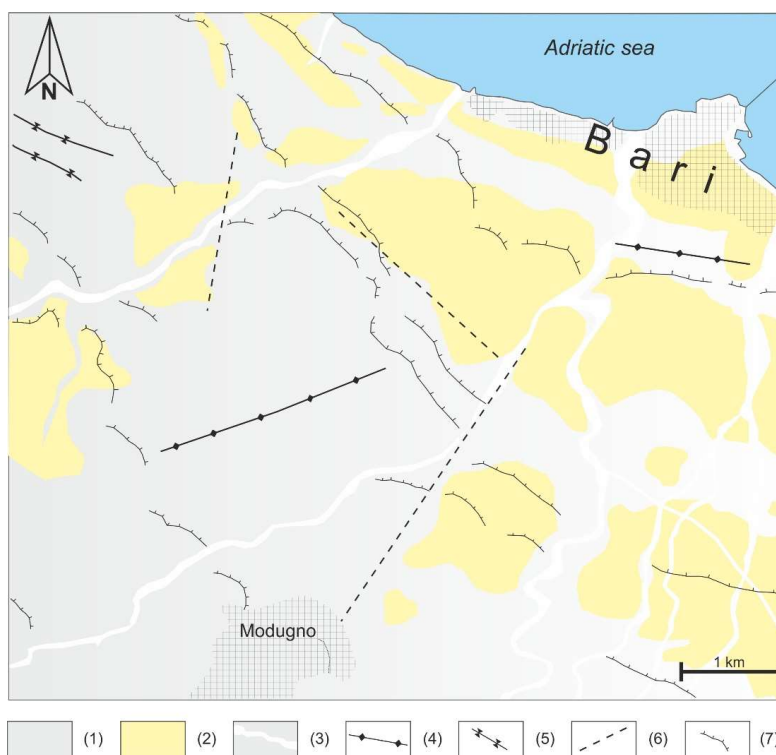
265 Moreover, the irregular spatial distribution of the fractures and karstic channels renders the Bari  
266 aquifer very anisotropic. The hydraulic conductivity of this aquifer is generally estimated in  
267  $10^{-3}$  to  $10^{-4}$  m/s.

268 The groundwater flows toward the sea, under a low pressure, in different subparallel fractured  
269 layers separated by compact (i.e., not fractured) rock blocks.





270 In proximity to the coast, the carbonate (Mesozoic) stratum contains fresh water flowing in  
271 phreatic conditions and floating on underlying saltwater of continental intrusion. The location  
272 of the transition zone between fresh and salt water has thickness and position variable and  
273 changes over time depending on the distribution of the hydrostatic pressures of the system.



274  
275

276 **Figure 1. Simplified geological map of the area of Bari: (1) Calcare di Bari formation (Cretaceous); (2) Calcareniti di**  
277 **Gravina formation (Lower Pleistocene); (3) hydrographic network; (4) anticlinal axis; (5) syncline axis; (6) fault**  
278 **(uncertain); (7): escarpment.**

279

### 280 **Hydrologic and hydrogeologic water budget**

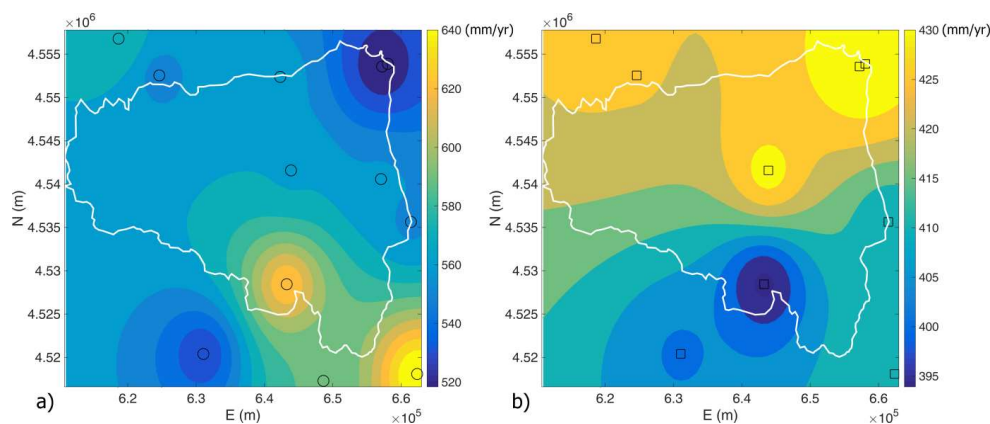
281 By means of the hydrologic and hydrogeologic water budget of the subtended basin the  
282 effective infiltration has been estimated.

283 Climatic data registered in the thermopluviometric stations present in the area have been  
284 elaborated and the average rainfall module and the monthly evapotranspiration have been  
285 calculated for the three decades 1974-2005.

286 12 climatic stations have been considered (Bari – hydrographic station, Bari – observatory  
287 station, Bitonto, Grumo appula, Adelfia, Casamassima, Mercadante, Ruvo di Puglia, Corato,  
288 Altamura, Santeramo, Gioia del Colle) and for each station and the monthly rainfall and



289 evapotranspiration map has been realised by means of the *Inverse distance weighting* algorithm.  
290 The latter has been estimated by means of Thornthwaite method applying a crop coefficient of  
291 0.40.  
292 The hydrologic and hydrogeologic basin have been defined on the basis of literature data and  
293 the regional thematic cartography.  
294 The lithotypes in the study area are principally limestones and calcarenites with secondary  
295 permeability, characterised by a high transmissivity. The zones in proximity of tectonic  
296 structures create preferential flow paths but at the same time generate a dismemberment of the  
297 aquifer that could not be able to feed the flow downstream. Because of that it proves to be  
298 difficult to carry out a zonation of recharge areas and therefore a constant run off coefficient of  
299 0.10 has been considered for the whole basin. In Figure 2 the map of the a) annual precipitation and  
300 b) real evapotranspiration evaluated for the hydrological basin of the study area is shown.



301  
302 **Figure 2.** Map of a) annual precipitation b) real evapotranspiration evaluated for the hydrological basin of the study  
303 area.

304

### 305 **Well performance tests: step-drawdown tests**

306 98 long term step drawdown hydraulic tests have been analysed in the study area.

307 A step-drawdown test is a single-well test in which the well is pumped at a low constant  
308 discharge rate until the drawdown within the well stabilizes.

309 Step drawdown tests can be used to evaluate the characteristics of the well and its immediate  
310 environment. Unlike the aquifer test, it is not designed to produce reliable information  
311 concerning the aquifer, even though it is possible to estimate the transmissivity of the immediate  
312 surroundings of the catchment. This test determines the critical flow rate of the well, as well as  
313 the various head-losses and drawdowns as functions of pumping rates and times. Finally, it is



314 designed to estimate the well efficiency, to set an exploitation pumping rate and to specify the  
315 depth of installation of the pump.

316 The total drawdown at a pumping well is given by:

$$317 \quad s = (A_1 + A_2) \cdot Q + B \cdot Q^2 \quad (1)$$

318 Where  $s$  (L) represents the registered drawdown,  $Q$  ( $L^3T^{-1}$ ) the pumped flow rate,  $A_1$  ( $TL^{-2}$ ) is  
319 the linear aquifer loss coefficient,  $A_2$  ( $TL^{-2}$ ) e  $B$  ( $T^2L^{-5}$ ) = are respectively the linear and  
320 nonlinear well-loss coefficients.

321 This equation can be explicited in terms of aquifer transmissivity  $T$  ( $L^2T^{-1}$ ), the transmissivity  
322 of damage zone  $T_{SKIN}$  ( $L^2T^{-1}$ ) and of the nonlinear term  $\beta$  ( $T^2L^{-4}$ ) (Cherubini & Pastore, 2011):

$$323 \quad s = \left[ \frac{1}{T2\pi} \ln\left(\frac{R}{r_w}\right) + \frac{1}{2\pi} \left( \frac{1}{T_{SKIN}} - \frac{1}{T} \right) \ln\left(\frac{r_{SKIN}}{r_w}\right) \right] Q + \left[ \frac{\beta}{4\pi^2} \left( \frac{1}{r_w} - \frac{1}{R} \right) \right] Q^2 \quad (2)$$

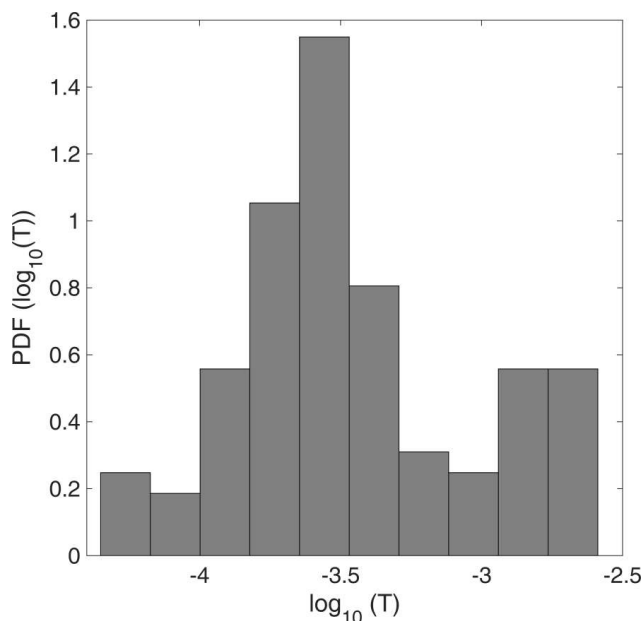
324 Where  $r_w$  (L) represents the well radius,  $r_{SKIN}$  (L) the radius of the damage zone,  $R$  (L) the radius  
325 of influence of the well.

326 The total drawdown is formed of three components: the hydraulic component of the aquifer  
327 assuming valid Thiem function, a skin function presented by Cooley and Cunningham (1979)  
328 assuming that the transmissivity and the radius of the damage zone are respectively equal to:  
329  $T_{SKIN} = T / 2$  e  $r_{SKIN} = 2r_w$ ; and a contribution related to nonlinear losses introduced by Wu  
330 (2001).

331 The radius of influence of the well is obtained by means of Sichart equation:

$$332 \quad R = 3000 \cdot s \cdot \sqrt{K} \quad (3)$$

333 In figure 3 is reported the statistical distribution of the estimated transmissivity values along  
334 the study area.



335  
336 **Figure 3. Statistical distribution of  $\log_{10}(T)$ .**

337

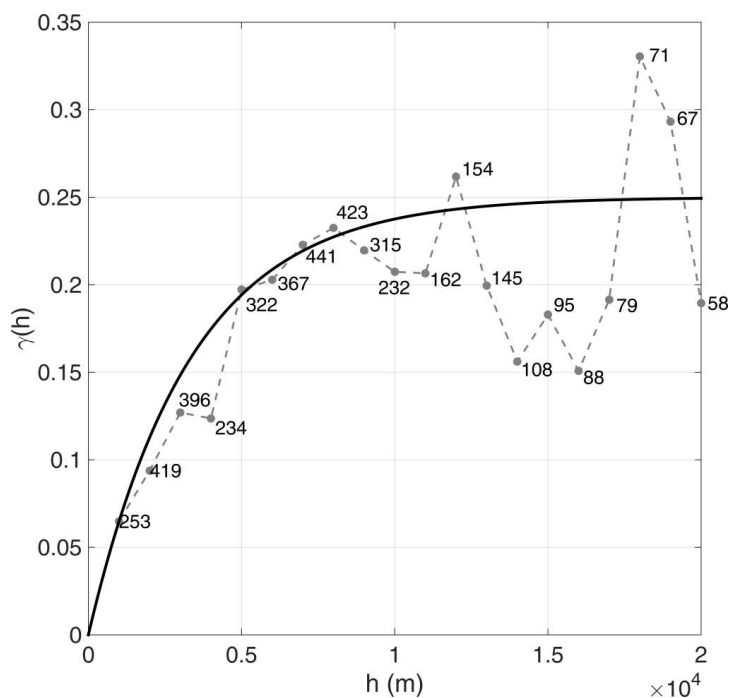
### 338 **Linear model of regionalization of Transmissivity**

339 The geostatistical analysis has been carried out on the  $\log_{10}$  transmissivity values using the open  
340 source code S-GemS (Remy, 2004).

341 The experimental variogram, which provides a description of how the data are related  
342 (correlated) with distance, has been calculated (Figure 4). Because the kriging algorithm  
343 requires a positive definite model of spatial variability, the experimental variogram cannot be  
344 used directly. Instead, a model must be fitted to the data to approximately describe the spatial  
345 continuity of the data. An exponential model has been used to fit the experimental variogram  
346 described by the function:

$$347 \quad \gamma(h) = C \left[ 1 - \exp\left(-\frac{h}{a}\right) \right] \quad (4)$$

348 Where  $C$  represents the variance (sill),  $h$  [L] the lag and  $a$  [L] the correlation length (range). In  
349 our case  $C$  assumes a value of 1.2 and  $a$  of 10000 m.



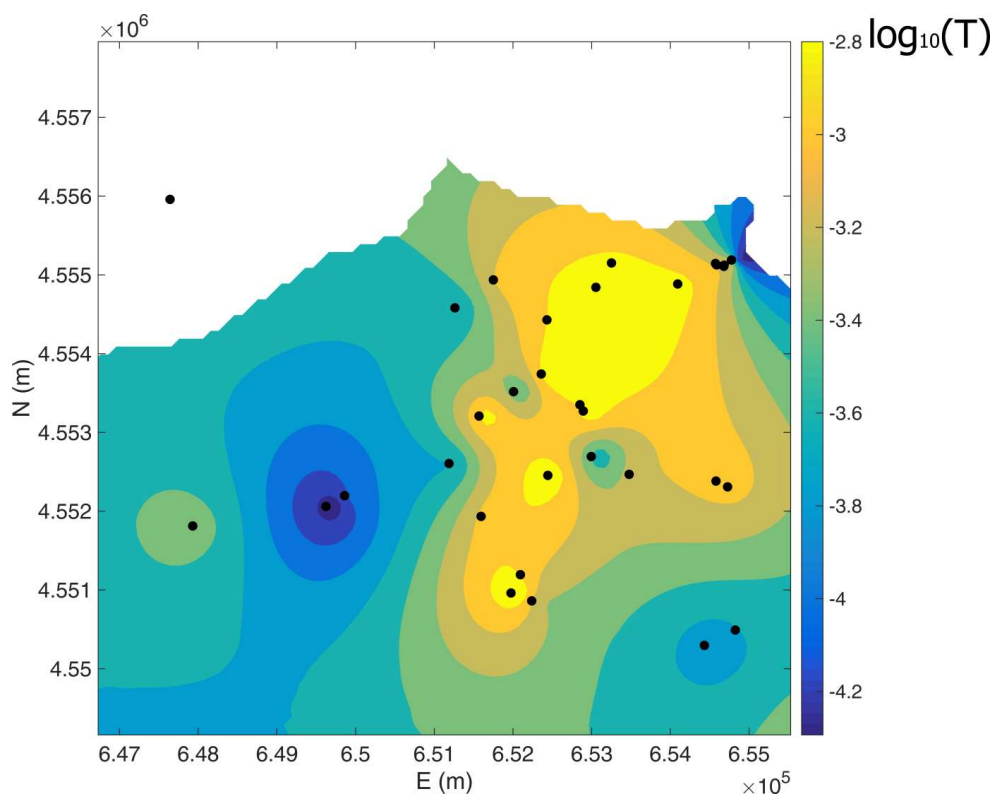
350

351 **Figure 4.** Omnidirectional experimental variogram fitted with an exponential model, sill = 1.2, range = 10000 m.

352

353 Figure 5 shows the ordinary Kriging interpolation of  $\log_{10}(T)$ .

354



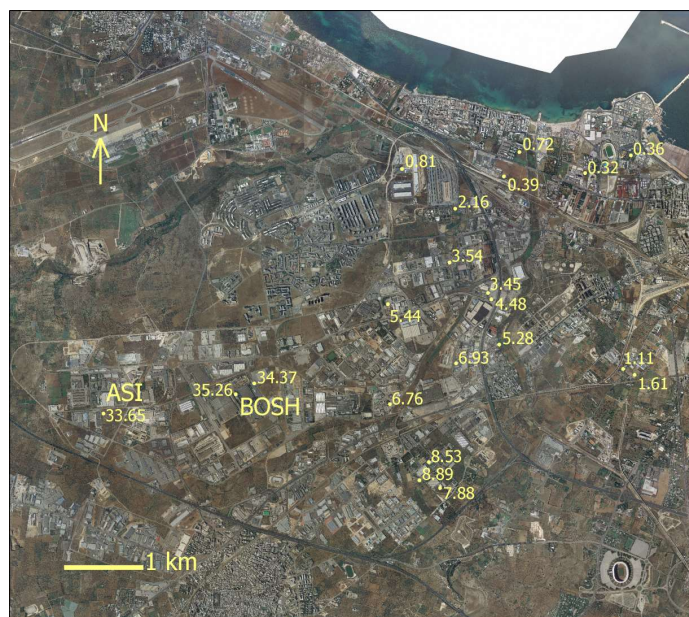
355

356 **Figure 5. Ordinary Kriging interpolation of  $\log_{10}(T)$ .**

357

### 358 **Analysis of piezometric data**

359 Figure 6 shows the spatial distribution of hydraulic heads on the basis of 2012 sampling  
360 campaign. A global trend in the direction of groundwater flow from SW to NE is evident. A  
361 relevant aspect is the presence of high hydraulic head values in proximity of ASI and Bosch  
362 wells. A possible explanation for this could be the presence of a zone of poor connection of  
363 groundwater flow patterns in correspondence of that zone. The aquifer transmissivity in that  
364 zone is of the order of  $10^{-5}$  m/s. The trend observed in the hydraulic gradient confirms the  
365 increase of the aquifer transmissivity from upstream to downstream, in fact the tests carried out  
366 in proximity of the coast have returned a transmissivity value of  $10^{-2}$  m/s.



367  
368  
369

Figure 6. Measured piezometric heads (m, slm) from February 2012 monitoring campaign

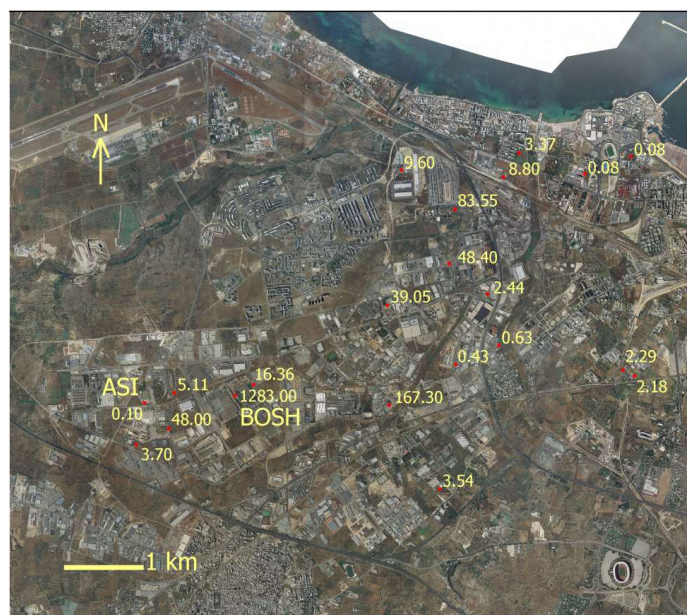
### 370 Analysis of the scenario of contamination for the study area

371 The various monitoring campaigns carried out have showed a contamination of Chlorinated  
372 Aliphatic Hydrocarbons which, unlike petroleum products, are denser than water and can exist  
373 as Dense Non-Aqueous Phase Liquids (DNAPLs).

374 The presence of two hot spot areas has been detected, located upstream of the groundwater  
375 flow, coherently with the state of contamination detected downstream.

376 Figure 7 shows the location of the detected contamination ( $\mu\text{g/l}$ ).

377 The pollution indicator has been chosen on the basis of the toxicologic and carcinogenic  
378 parameters, the solubility, the sorption coefficient and the maximum detected contaminant  
379 concentration. On the basis of the results of this screening the Tetrachloroethylene (PCE) has  
380 the highest concentration as well as low values of Reference Dose Factors (RfD) and Slope  
381 Factors (SF).



382  
 383 **Figure 7. Location of the detected contamination ( $\mu\text{g/l}$ ).**  
 384

385 **Parallel rough-walled fracture model**

386 The simplest model of flow through rock fractures is the parallel plate model (Huit, 1955; Snow,  
 387 1965) which conceptualises the fractured medium as made by a set of smooth parallel plates  
 388 having the same hydraulic aperture  $b_{eq}$  (L) that are separated by a uniform distance. This is  
 389 actually the only geometrical fracture model for which an exact calculation of the hydraulic  
 390 conductivity is possible.

391 Natural fractures present rough walls and complex geometries. Nonlinear flow may occur  
 392 through rough-walled rock fractures as a consequence the inertial effect dominate the flow  
 393 dynamics giving rise a deviation from darcy's law. Fluid flow through a set of natural fracture  
 394 planes can be expressed using the Darcy-Weisbach equation:

395 
$$\frac{dh}{dx} = -\frac{f}{D} \frac{v^2}{2g} \quad (5)$$

396 Where  $D$  (L) represents the hydraulic diameter ( $2b$  for the parallel plate model),  $f$  the Darcy –  
 397 Weisbach coefficient,  $h$  (L) is the hydraulic head,  $x$  (L) is the distance and  $v$  ( $\text{LT}^{-1}$ ) is the average  
 398 velocity in fracture calculated as:

399 
$$v = \frac{q}{n_f b} \quad (6)$$

400 Where  $q$  ( $\text{L}^2\text{T}^{-1}$ ) is the volumetric flow rate per unit length of fractures.





401 The Darcy – Weisbach equation can be rewritten in terms of volumetric flow per unit length:

$$402 \quad \bar{q} = - \left[ n_f b \frac{\sqrt{\frac{4b}{f} g}}{\sqrt{|\nabla h|}} \right] \nabla h \quad (7)$$

403 The term in square bracket represents the equivalent hydraulic transmissivity  $T_{eq}(f, \nabla h)$  of the  
404  $n_f$  rough - walled fractures.

405 The Darcy-Weisbach coefficient or friction factor depends of the flow regime. In the case of  
406 smooth-walled fracture and linear flow regime  $f$  is equal to:

$$407 \quad f = \frac{96}{\text{Re}} \quad (8)$$

408 Where Re represents the Reynolds number:

$$409 \quad \text{Re} = \frac{\rho v D}{\mu} \quad (9)$$

410 Substituting equation (8) in equation (7) the cubic law (Witherspoon et al., 1980) where  $q$  is  
411 proportional to the cubic power of the fracture aperture is obtained:

$$412 \quad q = n_f \frac{\rho g}{\mu} \frac{b^3}{12} \quad (10)$$

413 The cubic law is not always adequate to represent the flow process in natural fractures, a  
414 deviation from linearity can be observed.

415 The friction factor depends from the flow regime described by the Reynolds number and can  
416 be presented with the following relationship found by Nazridoust et al. (2006):

$$417 \quad f = \frac{123}{\text{Re}} \left( 1 + 0.12 \text{Re}^{0.687} \right) \quad (11)$$

418

### 419 **Inverse flow modeling**

420 Inverse modelling is a technique used to estimate unknown model parameters using as input  
421 data punctual values of the state variables (hydraulic head, flow). Generally, in real problems  
422 the number of parameters to estimate ( $n$ ) is higher than the number of measured values ( $m$ ). For  
423 example, this is the case of mapping hydraulic transmissivity values varying continuously in  
424 space.

425 For underdetermined inverse problems of this kind the objective function ( $L$ ) can be written in  
426 this way:

$$427 \quad L(\mathbf{y}, \mathbf{s}) = L_{fitness}(\mathbf{y}, \mathbf{s}) + L_{penalty}(\mathbf{s}) \quad (12)$$



428 Where  $\mathbf{s}$  represents the vector of measured values of state variables (es. hydraulic  
429 transmissivity),  $\mathbf{y}$  represents the vector of parameter values.

430 The *fitness function* responds to maximum likelihood criteria between the observed and the  
431 simulated values and can be written as:

$$432 \quad L_{fitness}(\mathbf{y}, \mathbf{s}) = (\mathbf{y} - \mathbf{h}(\mathbf{s}))^T \mathbf{R}^{-1} (\mathbf{y} - \mathbf{h}(\mathbf{s})) \quad (13)$$

433 Where  $\mathbf{h}$  represents the model that, starting from the parameter vector, estimates the state  
434 variable,  $\mathbf{R}$  is the measurement error covariance matrix. Generally this function can be reduced  
435 to the square root of the sum of the squared difference between the measured and simulated  
436 (RMSE):

$$437 \quad L_{fitness} = \frac{\|\mathbf{y} - \mathbf{h}(\mathbf{s})\|^2}{\Delta H^2} \quad (14)$$

438 Where  $\Delta H$  represents a parameter of accuracy of observed data.

439 The *penalty function* is used to discriminate the solutions with values of the fitness function  
440 comparable by means of geostatistical criteria (Kitanidis, 1995):

$$441 \quad L_{penalty} = (\mathbf{s} - \mathbf{X}\beta)^T \mathbf{Q}^{-1} (\mathbf{s} - \mathbf{X}\beta) \quad (15)$$

442 Where  $\mathbf{Q}$  represents the spatial covariance matrix,  $\mathbf{X}$  is a unit vector and  $\beta$  is the mean of the  
443 values of the parameters. The penalty function can be rewritten eliminating  $\beta$ :

$$444 \quad L_{penalty} = \mathbf{s}^T \mathbf{G} \mathbf{s} \quad \mathbf{G} \equiv \mathbf{Q}^{-1} - \frac{\mathbf{Q}^{-1} \mathbf{X} \mathbf{X}^T \mathbf{Q}^{-1}}{\mathbf{X}^T \mathbf{Q}^{-1} \mathbf{X}} \quad (16)$$

445 The common assumption is that the spatial distribution of the parameters follows the  
446 geostatistical distribution defined by the variogram. Under this hypothesis the covariance  
447 matrix present in the penalty function can be defined as:

$$448 \quad Q_{ij} = 2\gamma(|x_i - x_j|) \quad i, j = 1, \dots, n \quad (17)$$

449

#### 450 **Solute transport modeling**

451 Solute transport in fracture neglecting the effect of matrix diffusion and the chemical reactions  
452 can be described by the following advection dispersion equation:

$$453 \quad \frac{\partial c}{\partial t} + \bar{\mathbf{v}} \cdot \nabla c = \nabla \cdot (\mathbf{D} \nabla c) \quad (18)$$

454 Where  $c$  ( $\text{ML}^{-3}$ ) is the concentration of solute and  $\mathbf{D}$  ( $\text{L}^2\text{T}^{-1}$ ) is the symmetric dispersion tensor  
455 having the following components:



$$\begin{aligned}
 D_{xx} &= (\alpha_L v_x^2 + \alpha_T v_y^2) / |v| \\
 456 \quad D_{yy} &= (\alpha_T v_x^2 + \alpha_L v_y^2) / |v| \\
 D_{xy} &= (\alpha_L - \alpha_T) v_x v_y / |v|
 \end{aligned} \tag{19}$$

457 Where  $\alpha_L$  (L) and  $\alpha_T$  (L) are the longitudinal and transverse dispersion coefficients respectively.

458 In order to solve the advective transport equation a numerical Lagrangian particle based random

459 walk method is implemented. The solute plume is discretized into a finite number of particles.

460 For pure advective transport the particle moves along the flow lines. In order to represent

461 dispersion phenomena, the random walk method adding a random displacement to each

462 particle, independently of the other particles, in addition to advective displacement.

463 For a given time step  $\Delta t$ , considering the tensorial nature of the dispersion and the spatially

464 variable velocity field each, particle moves according to:

$$\begin{aligned}
 465 \quad x_p(t + \Delta t) &= x_p(t) + v'_x \Delta t + Z_1 \sqrt{2D_L \Delta t} \frac{v_x}{|v|} - Z_2 \sqrt{2D_T \Delta t} \frac{v_y}{|v|} \\
 y_p(t + \Delta t) &= y_p(t) + v'_y \Delta t + Z_1 \sqrt{2D_L \Delta t} \frac{v_y}{|v|} + Z_2 \sqrt{2D_T \Delta t} \frac{v_x}{|v|}
 \end{aligned} \tag{20}$$

466 With:

$$\begin{aligned}
 v'_x &= v_x + \frac{\partial D_{xx}}{\partial x} + \frac{\partial D_{xy}}{\partial y} \\
 467 \quad v'_y &= v_y + \frac{\partial D_{xy}}{\partial x} + \frac{\partial D_{yy}}{\partial y} \\
 D_L &= \alpha_L |v| \\
 D_T &= \alpha_T |v|
 \end{aligned} \tag{21}$$

468 For steady – state flow and for a source constant intensity, the assumption that the particles  $N$

469 released in time interval  $(t_1, t_1 + \Delta t)$  follow exactly the same random trajectories of the particles

470  $N$  released during the previous interval  $(t_1, t_1 - \Delta t)$  is possible. Under this assumption only  $N$

471 particles are needed to simulate the location of the particles at previous time step.

472

### 473 **Flow modeling**

474 The numerical code MODFLOW coupled with the inverse model approach presented in the  
475 previous section has been used to model groundwater flow.

476 The numerical simulations have been carried out on a two-dimensional domain of 968.7 Km<sup>2</sup>.

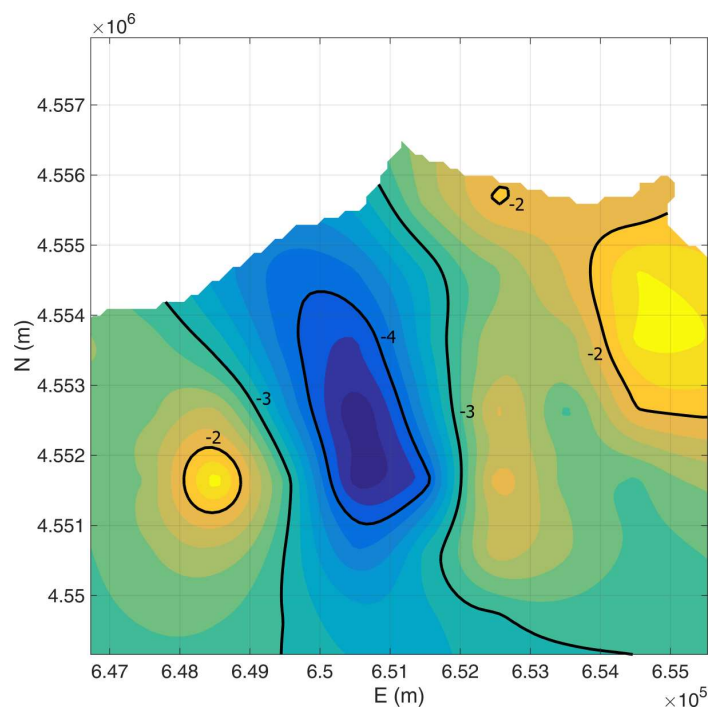
477 The domain has been discretised by means of a structured grid of 100 m size with.

478 In correspondence of the coast line a first type boundary condition has been imposed ( $h = 0$  m),

479 along the detected watershed a second type boundary condition ( $q = 0$  m<sup>2</sup>/s), the recharge from



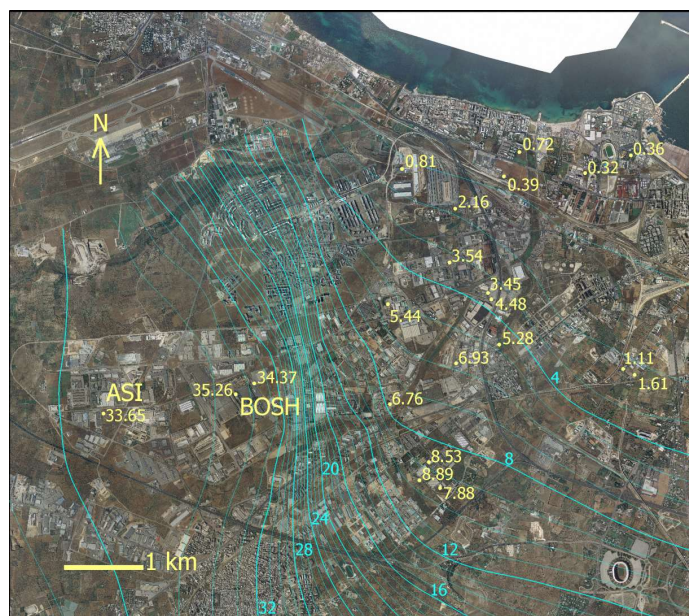
480 upstream is simulated by means of a first type boundary condition where the hydraulic heads  
481 are equal to the detected regional values  $h = 32 - 41$  m (Piano di Tutela delle Acque Regione  
482 Puglia, Tav. 6.2 <http://old.regione.puglia.it/index.php?page=documenti&id=29&opz=getdoc>).  
483 A second type boundary condition on the whole simulation domain has been imposed that  
484 concerns the mean effective infiltration calculated from the hydrologic budget  $q = 0.037$   $\text{md}^{-1}$ .  
485 The algorithm of inverse modelling has been applied to carry out the estimation of the spatial  
486 distribution of the equivalent transmissivity (Figure 8) on the basis of the observed hydraulic  
487 head (vector  $\mathbf{y}$ ), the regionalization model (matrix  $\mathbf{Q}$ ) described by the variogram of the  
488 logarithmic of the hydraulic transmissivity determined in the previous section.  
489 The inverse model algorithm follows those steps. 1) Starting from a conditional simulation of  
490 the log of  $T_{eq}$  determined by means of the hydraulic tests conducted in the area. 2) A set of pilot  
491 points are chosen in the area using a regular spaced criteria and the value of  $T_{eq}$  has been  
492 determined for each pilot points (vector  $\mathbf{s}$ ). 3) By means of the Ordinary Kriging interpolation  
493 of the pilot points the map of  $T_{eq}$  is obtained and represents the input datum of the flow  
494 numerical model. 4) The hydraulic head has been determined using the flow numerical model  
495 (vector  $\mathbf{h}$ ) and the values of the objective function has been determined using the equation ().  
496 5) the values of  $T_{eq}$  are updated for each pilot points.  
497 Using Levenberg–Marquardt algorithm the values of  $T_{eq}$  for each pilot points is updated as long  
498 as the objective function is minimized.  
499 Figure 9 shows the results obtained from the flow model in steady state condition, calibrated  
500 with the measurement campaign of February 2012 (Table 1).  
501 Table 2 shows the data of model calibration and Figure 10 shows the graph of the calibration.  
502 The outcomes of the calibration are satisfactory. The comparison between the simulated and  
503 observed datum has given a mean absolute residual equal to 0.57 m, an RMSE equal to 4.57 m,  
504 a correlation coefficient  $r^2$  equal to 0.997. In the following figures and tables are shown the  
505 results for the flow model.



506

507

Figure 8. Map of  $\log_{10}$  of aquifer transmissivity determined by means of inverse modelling algorithm.



508

509

Figure 9. Map of simulated hydraulic heads (blue line)

510



Name	Obs. Head (m)	Computed Head (m)	Residual Head (m)
P10	4.480	3.682	-0.798
L1-S	5.278	4.835	-0.443
P11	1.611	2.205	0.594
P19	1.110	2.217	1.107
P14	0.321	0.515	0.194
L2-S	0.722	0.466	-0.256
P4	0.386	0.801	0.415
L3-S	2.163	1.870	-0.293
P3	5.441	5.519	0.078
P16	3.536	3.315	-0.221
L4-S	3.450	3.567	0.117
P18	6.926	5.851	-1.075
L5-S	33.649	35.587	1.938
L8-S	8.532	8.809	0.277
L7-S	7.880	9.516	1.636
L6-S	8.892	9.651	0.759
P13	0.807	1.281	0.474
L9	0.705	0.236	-0.469
L10	0.167	0.276	0.109
L11	0.317	0.279	-0.038
L12	0.360	0.245	-0.115
L13	0.418	0.144	-0.274
L14-S	34.370	33.776	-0.594
L15-S	35.260	34.477	-0.783
P2	6.760	7.865	1.105

511 **Table 1. Comparison between the observed and simulated hydraulic heads with related residual, relatively to the**  
512 **measurement campaign of February 2012.**

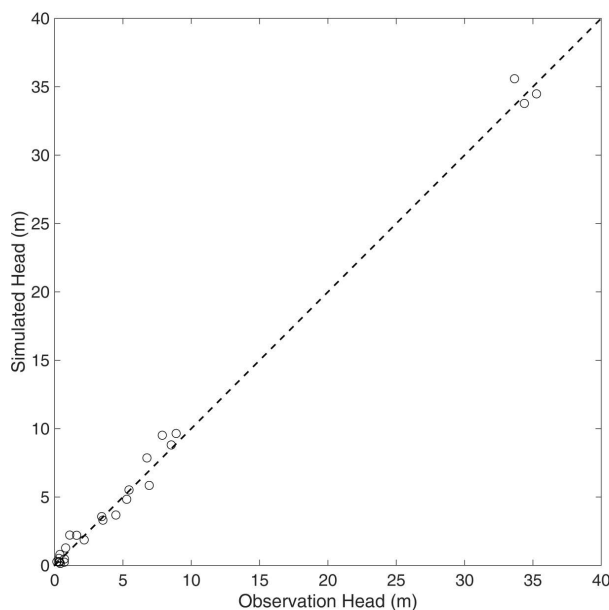
513

514

<b>Mean Residual</b>	-0.138
<b>Mean Absolute Residual</b>	0.566
<b>Root Mean Squared Residual</b>	0.743
<b>Sum of Squared Weighted Residual</b>	4.571

515

516 **Table 2. Data of model calibration.**



517

518 **Figure 10. Graph of the calibration.**

519

520 Once obtained the equivalent hydraulic transmissivity map and assuming a values of the  
 521 number of set of fractures  $n_f$  the spatial distribution of the mean equivalent aperture and the  
 522 velocity field can be obtained.

523 Assuming valid the cubic law the mean equivalent aperture can be obtained as:

$$524 \quad b_{eq} = \sqrt[3]{12 \frac{T_{eq} \mu}{n_f \rho g}} \quad (22)$$

525 The velocity field resulting:

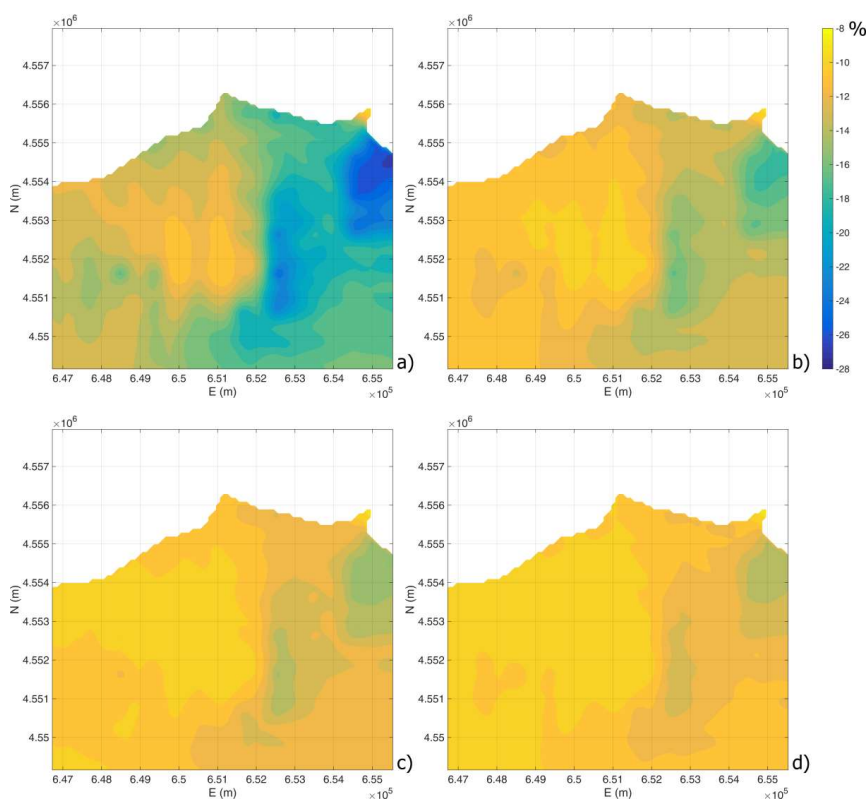
$$526 \quad \begin{aligned} v_x &= -\frac{\rho g}{\mu} \frac{b_{eq}^2}{12} h_x \\ v_y &= -\frac{\rho g}{\mu} \frac{b_{eq}^2}{12} h_y \end{aligned} \quad (23)$$

527 Whereas assuming valid the Darcy – Weisbach equation the mean equivalent aperture and the  
 528 flow field can be obtained by means of the following iterative steps starting from the values of  
 529  $b_{eq}$ ,  $v_x$  and  $v_y$  previously evaluated:



$$\begin{aligned}
 \text{Re}^k &= \frac{\rho |v^k| 2b_{eq}^k}{\mu} \\
 f^{k+1} &= \frac{123}{\text{Re}^k} \left( 1 + 0.12 (\text{Re}^k)^{0.687} \right) \\
 b_{eq}^{k+1} &= \sqrt[3]{\frac{T_{eq}}{n_f^2} \frac{f^{k+1}}{4g} |\nabla h|} \\
 v_x^{k+1} &= -\frac{\sqrt{\frac{4b_{eq}^{k+1}}{f^{k+1}} g}}{\sqrt{|\nabla h|}} h_x \\
 v_y^{k+1} &= -\frac{\sqrt{\frac{4b_{eq}^{k+1}}{f^{k+1}} g}}{\sqrt{|\nabla h|}} h_y
 \end{aligned} \tag{24}$$

531 Figure 11 shows the relative percentage of error on the flow velocity for different number of  
 532 fractures.



533

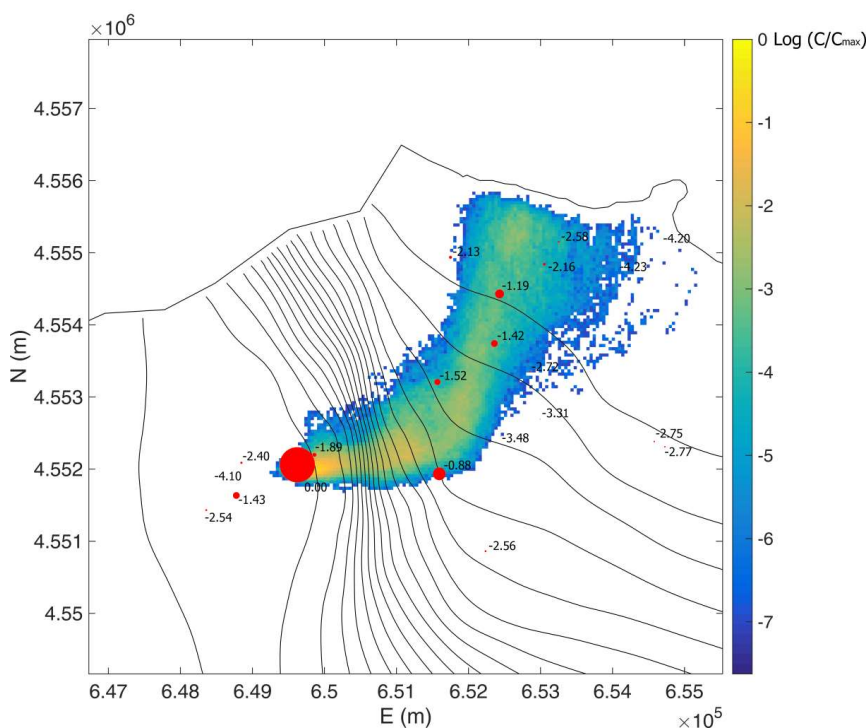




534 **Figure 11. Relative percentage of error on the flow velocity for different number of fractures: a)  $n_f = 4$ ; b)  $n_f = 12$ ; c)  $n_f = 20$ ; d)  $n_f = 28$ .**

### 536 **Detection of the sources of contamination**

537 A particle tracking transport method has been applied for the simulation of contaminant  
538 transport. The obtained simulation scenario proves to be compatible with the observed one and  
539 therefore it is possible to assume that the sources of contamination are located in  
540 correspondence of the observed hot spot (Figure 12).



541 **Figure 12. Steady state distribution of hypothetical contamination using the random walk model with the source**  
542 **contamination localized in correspondence of the hot spot of the contamination considering a number of fracture of  $n_f$**   
543 **= 20 and a longitudinal and transversal dispersion coefficient equal to  $\alpha_L = 70$  m and  $\alpha_T = 7$  m.**

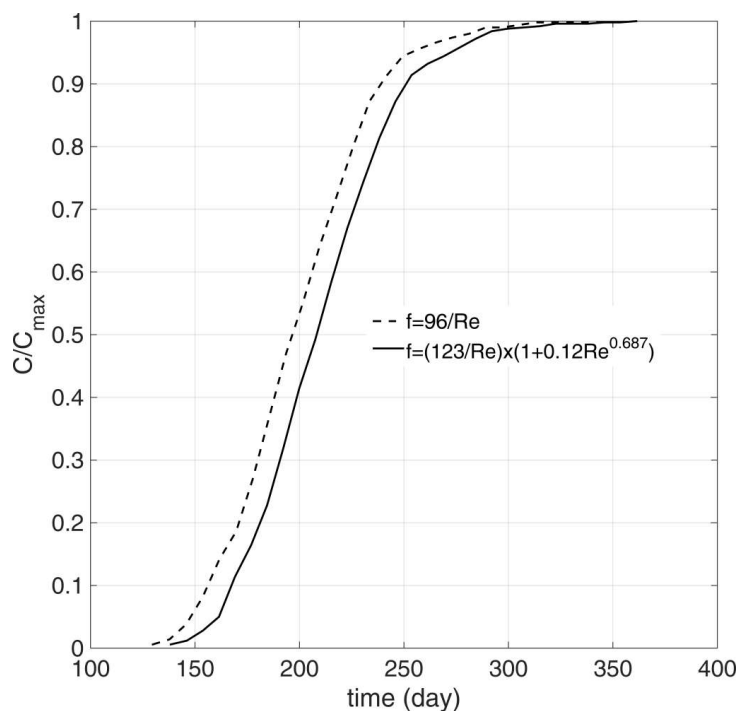
545  
546 Figure 13 shows the breakthrough curves of hypothetical continuous contamination released in  
547 correspondence of the hot spot, determined for linear and nonlinear flow model, evaluated at  
548 the downstream boundary for  $n_f = 20$ . The nonlinear model shows a delay in the breakthrough  
549 compared with the linear one. This is coherent with what detected by Cherubini et al (2014)  
550 who found a delay in advective solute transport for a nonlinear flow model in a fractured rock  
551 formation respect to the linear flow assumption.



552 In fracture networks, the presence of nonlinear flow plays an important role in the distribution  
553 of the solutes according to the different pathways. In fact, the energy spent to cross the path  
554 should be proportional to the resistance to flow associated to the single pathway, which in  
555 nonlinear flow regime is not constant but depends on the flow rate. This means that by changing  
556 the boundary conditions, the resistance to flow varies and as a consequence the distribution of  
557 solute in the main and secondary pathways also changes, giving rise to a different behavior of  
558 solute transport (Cherubini et al. 2014).

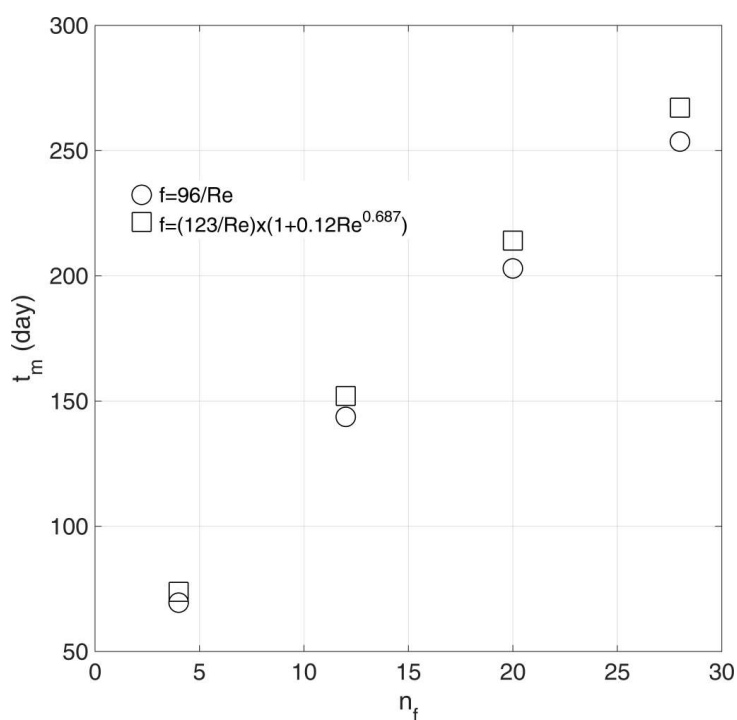
559 Figure 14 shows the mean travel time at varying number of fractures for the linear and nonlinear  
560 model. With increasing number of fractures, the travel time increases in a linear way, because  
561 the cross section area increases as well. The travel time for the nonlinear model is higher than  
562 the linear assumption, coherently with the previous finding.

563



564

565 **Figure 13. Breakthrough curves of hypothetical continuous contamination released in correspondence of the hot spot,**  
566 **determined for linear and nonlinear flow model, evaluated at the downstream boundary.**



567

568 **Figure 14. Mean travel time  $t_m$  at varying the number of fractures  $n_f$  for linear and nonlinear model.**

## 569 **Conclusions**

570 The present study is aimed at analysing the scenario of groundwater contamination (by  
571 investigating the hotspots) of the industrial area of Modugno (Bari –Southern Italy) where the  
572 limestone aquifer has a fractured and karstic nature.

573 The presence of hot spot areas has been detected, located upstream of the groundwater flow,  
574 coherently with the state of contamination detected downstream.

575 A rough walled parallel plate model has been implemented and calibrated on the basis of  
576 piezometric data and has coupled a geostatistical analysis to infer the values of the equivalent  
577 aperture. Using the random walk theory, the steady state distribution of hypothetical  
578 contamination with the source contamination at the hot spot has been carried out.

579 The flow and transport model have well reproduced the flow pattern and have given a pollution  
580 scenario that is compatible with the observed one.

581 From an analysis of the flow and transport pattern it is possible to infer that the anticline  
582 affecting the Calcare di Bari formation in directions ENE-WSW influences the direction of flow  
583 as well as the propagation of the contaminant.



584 The results also show that the presence of nonlinear flow influences advection, in that it leads  
585 to a delay in solute transport respect to the linear flow assumption. Moreover, the distribution  
586 of solute according to different pathways is not constant but is related to the flow rate  
587 This is due to the non-proportionality between the energy spent to cross the path and the  
588 resistance to flow for fractured media, which affects the distribution of the solutes according to  
589 the different pathways.  
590 The obtained results represent the fundamental basis for a detailed study of the contaminant  
591 propagation in correspondence of the hot spot area in order to find the best clean up strategies  
592 and optimize any anthropic intervention on the industrial site  
593 Future developments of the current study will be to implement a transient model and to include  
594 the density dependent flow into the simulations.

595

596

## 597 **References**

## 598 **References**

- 599 Baker, W. J. Flow in fissured formations. *Proceedings of 4th Worm Petroleum Congress* **1955**.  
600 Carlo Colombo, Rome, 379-393.
- 601 Berkowitz, B.; Kosakowski, G.; Margolin, G.; Scher, H. Application of Continuous Time  
602 Random Walk Theory to Tracer Test Measurements in Fractured and Heterogeneous Porous  
603 Media Ground. *Water* **2001**, 39(4), 593-603.
- 604 Brush, D.J.; Thomson, N.R. Fluid flow in synthetic rough-walled fractures: Navier-Stokes,  
605 Stokes, and local cubic law simulations. *Water Resour. Res.* **2003**, 39(4), 1085.
- 633 Bourke, P. J. Channeling of flow through fractures in rock, in *Proceedings of GEOVAL-1987*  
634 *International Symposium, Swedish Nuclear Power Inspectorate (SKI), Stockholm, 1987*, 1.11,  
635 67 – 177.
- 636 Cherubini C. A modeling approach for the study of contamination in a fractured aquifer.  
637 *Geotechnical and geological engineering, Springer, Netherlands, 2008*, 26/5, 519–533.
- 638 Cherubini, C., Pastore, N., Francani, V. Different approaches for the characterization of a  
639 fractured karst aquifer. In: *World scientific and engineering academy and society. transactions*  
640 *on fluid mechanics, Wisconsin-Usa, 2008*, 1/3, 29–35.
- 641 Cherubini, C., Giasi, C., Pastore, N. Fluid flow modeling of a coastal fractured karstic aquifer  
642 by means of a lumped parameter approach. *Environ Earth Sci*, **2013**, 70,2055–2060.



- 643 Cherubini, C., Pastore, N. Modeling contaminant propagation in a fractured and karstic aquifer,  
644 *Fresenius Environmental Bulletin*, **2010**, 19/9, 1788-1794.
- 645 Dentz, M., Kang, P. K., Le Borgne, T. Continuous Time Random Walks for Non-Local Radial  
646 Solute Transport, *Advances in Water Resources Volume 82, August 2015*, 16-26.
- 647 Diersch, H.J.G. FEFLOW finite element subsurface flow and transport simulation system—  
648 User’s manual/Reference manual/White papers. *Release 5.1. WASY Ltd, Berlin, 2002*.
- 649 Elliott, G. M., Brown, E. T. Laboratory measurement of the thermo-hydro-mechanical  
650 properties of rock. *Quarterly Journal of Engineering Geology*, **1988**, 21, 299-314.
- 651 Gale, J. A Numerical Field and Laboratory Study of Flow in Rocks with Deformable Fractures,  
652 *Sci. Ser. 72, Inland Waters Dir., Water Resources Branch, Ottawa, Ontario, Canada, 1977*.
- 653 Huitt, J.L. Fluid Flow in Simulated Fractures, *Amer. Inst. Chem. Eng. Journal*, **1956**, 2, 259-  
654 264.
- 655 Lee, J., Kang, J. M., Choe J. Experimental analysis on the effects of variable apertures on tracer  
656 transport, *Water Resour. Res.*, **2003**, 39/1, 1015.
- 657 Keller, A. High resolution, non-destructive measurement and characterization of fracture  
658 apertures, *Int. J. Rock Mech. Min. Sci.*, **1998**, 35/8, 1037 – 1050.
- 659 Keller, A. A., Roberts, P. V., Blunt M. J. Effect of fracture aperture variations on the dispersion  
660 of contaminants, *Water Resour. Res.*, **1999**, 35, 55 – 63.
- 661 Klimczak, C., Schultz, R. A., Parashar, R., Reeves D. M. Cubic law with aperture-length  
662 correlation: implications for network scale fluid flow. *Hydrogeology Journal*, **2010**, 18/4, 851–  
663 862.
- 664 Masciopinto, C., Palmiotta, D. Flow and Transport in Fractured Aquifers: New Conceptual  
665 Models Based on Field Measurements, *Transp Porous Media*, **2013**, 96/1, 117–133.
- 666 Masciopinto, C., Visino, F. Strong release of viruses in fracture flow in response to a  
667 perturbation in ionic strength: Filtration/retention tests and modeling. *Water Research*, **2017**,  
668 in press.
- 669 Masciopinto, C., Volpe, A., Palmiotta, D., Cherubini, C. A combined PHREEQC-2/parallel  
670 fracture model for the simulation of laminar/non-laminar flow and contaminant transport with  
671 reactions, *J. Contam. Hydrol.*, **2010**, 117, 94–108.
- 672 Neretnieks, I., Eriksen, T., Tahtinen P. Tracer movement in a single fissure in granitic rock:  
673 Some experimental results and their interpretation, *Water Resour. Res.*, **1982**, 18/4, 849 – 858.
- 674 Neuzil, C.E., Tracy, J.V. “Flow Through Fractures,” *Water Resources Research*, **1981**, 17/1  
675 191-199.



- 676 Oron, A.P., Berkowitz, B. Flow in rock fractures: The local cubic law assumption reexamined.  
677 *Water Resour. Res.*, **1998**, 34/11, 2811-2825.
- 678 Plouraboué, F., Kurowski, P. J., Hulin, P., Roux, S., Schmittbuhl J. Aperture of rough crack,  
679 *Phys. Rev.*, **1995**, 51, 1675 – 1685.
- 680 Plouraboué, F., Kurowski, P., Boffa, J.M., Hulin, J.P., Roux, S. Experimental study of the  
681 transport properties of rough self-affine fractures. *Journal of Contaminant Hydrology*, **2000**,  
682 46/3-4, 295-318.
- 683 Priest, S.D., Hudson, J.A. Discontinuity spacings in rock. *Int J Rock Mech Min Sci Geomech*  
684 *Abstr*, **1976**, 13, 135–148.
- 685 Pyrak-Nolte, L. J., Cook, N. G. W., Nolte D. Fluid percolation through single fractures,  
686 *Geophys. Res. Lett.*, **1988**, 15/11, 1247 – 1250.
- 687 Srinivasan, G., Tartakovsky, D.M., Dentz, M., Viswanathan, H., Berkowitz B., Robinson, B.A.  
688 Random walk particle tracking simulations of non-Fickian transport in heterogeneous media,  
689 *Journal of Computational Physics*, **2010**, 229, 4304–4314.
- 690 Tsang, Y. W., Tsang C. F. Channel model of flow through fractured media, *Water Resour. Res.*,  
691 **1987**, 23/3, 467-479.
- 702 Tsang, Y. W., Tsang C. F. Flow channeling in a single fracture as two-dimensional strongly  
703 heterogeneous permeable medium, *Water Resour. Res.*, **1989**, 25/9, 2076 – 2080.
- 720 Tsang, C.-F., Tsang, Y. W., Birkholzer, J., Moreno L. Dynamic channeling of flow and  
721 transport in saturated and unsaturated heterogeneous media, in Flow and Transport Through  
722 Unsaturated Fractured Rock, 2nd ed., *Geophys. Monograph, AGU, Washington, D.C.*, **2001**,  
723 42, 33 – 44.
- 724 Yeo, I.W., Ge, S. Applicable range of the Reynolds equation for fluid flow in a rock fracture,  
725 *Geosciences Journal*, **2005**, 9/4, 347-352.
- 726 Wang, L., Cardenas, M.B., Slotke, D.T., Ketcham, R.A., Sharp, Jr. J.M. Modification of the  
727 Local Cubic Law of fracture flow for weak inertia, tortuosity and roughness. *Water Resour.*  
728 *Res.*, **2015**, 51, 2064–2080.
- 729 Witherspoon, P. A., Wang, J. S. Y., Iwai, K., Gale, J. E. Validity of the cubic law for fluid flow  
730 in a deformable rock fracture. *Water Resources Research*, **1980**, 16, 1016-1034.
- 731 Snow, D.T. A Parallel Plate Model of Fractured Permeable Media, *Ph.D. Dissertation*,  
732 *University of California*, **1965**.
- 733 Snow, D. The Frequency and Apertures of Fractures in Rocks, *International Journal of Rock*  
734 *Mechanics and Mining Science*, **1970**, 7, 23-40.



- 735 Zimmerman, R. W., Bodvarsson, G.S. Hydraulic conductivity of rock fractures, *Transport in*  
736 *Porous Media*, **1996**, 23/1, 1–30.
- 737 Zhao J., Brown E.T. Hydro-thermo-mechanical properties of joints in the Carnmenellis granite,  
738 *Quarterly Journal of Engineering Geology*, **1992**, 25, 279-290.
- 739 Zheng, Q., Dickson, S.E., Guo, Y. On the appropriate “equivalent aperture” for the description  
740 of solute transport in single fractures: Laboratory-scale experiments, *Water Resour. Res.*, **2008**,  
741 44, W04502. doi:10.1029/2007WR005970
- 742 Antonellini M., Cilona A., Tondi E., Zambrano M., Agosta F. Fluid-flow numerical  
743 experiments of faulted porous carbonates, Northwest Sicily (Italy). *Marine and Petroleum*  
744 *Geology*, **2014**, 55, 186-201.
- 745 Bieniawski, Z.T. Engineering Rock Mass Classifications. *John Wiley & Sons, New York*, **1989**,  
746 251.
- 747 Billi A., Salvini F., Storti F. The damage zone-fault core transition in carbonate rocks:  
748 implications for fault growth, structure and permeability. *Journal of Structural Geology*, **2003**,  
749 25, 1779-1794.
- 750 Caine J.S., Foster C. Fault Zone Architecture and Fluid Flow: Insights from Field Data and  
751 Numerical Modeling. In: *Haneberg W., Mozley P., Moore J. & Goodwin L., Faults and*  
752 *Subsurface Fluid Flow in the Shallow Crust. Washington, D.C., American Geophysical Union*  
753 *Geophysical Monograph*, **1999**, 113, 101-127.
- 754 Caine J.S., Evans J.P., Foster C. Fault zone architecture and permeability structure. *Geology*,  
755 **1996**, 24, 1025-1028.
- 756 Pieri P., Sabato L., Spalluto L., Tropeano M. Note illustrative, Carta geologica d'Italia, scala  
757 1:50.000, Foglio 438 "Bari", *Progetto CARG, ISPRA*, **2010**.
- 758 Deere, D.U., Deere D.W. The rock quality designation (RQD) index in practice. In *Rock*  
759 *classification systems for engineering purposes, (ed. L. Kirkaldie), ASTM Special Publication*  
760 *Philadelphia: Am. Soc. Test. Mat.*, **1988**, 984, 91-101.
- 761 Doglioni C. The Puglia uplift (SE Italy) An anomaly in the foreland of the Apenninic  
762 subduction due to buckling of a thick continental lithosphere. *Tectonics*, **1994**, 13/5, 1309-1321.
- 763 Foster C.B., Evans J.P. Hydrogeology of thrust faults and crystalline thrust sheets: results of  
764 combines field and modelling studies. *Geophys. Res. Lett.*, **1991**, 18, 979-982.
- 765 Korneva I., Tondi E., Agosta F., Rusctichelli A., Spina V., Bitonte R., Di Cuia R. Structural  
766 properties of fractured and faulted Cretaceous platform carbonates, Murge Plateau (Southern  
767 Italy). *Marine and Petroleum Geology*, **2014**, 57, 312-326.



- 768 Parise M., Pascali V. Surface and subsurface environmental degradation in the karst of Apulia  
769 (southern Italy). *Environmental Geology*, **2003**, 44, 247–256.
- 770 Pieri P., Festa V., Moretti M., Tropeano M. Quaternary tectonic activity of the Murge area  
771 (Apulian foreland-Southern Italy). *Annali di Geofisica*, **1997**, 40, 1395-1404.
- 772 Rustichelli, A., Tondi, E., Agosta, F., Cilona, A., Giorgioni, M. Development and distribution  
773 of bed-parallel compaction bands and pressure solution seams in carbonates (Bolognano  
774 Formation, Majella Mountain, Italy). *J. Struct. Geol.*, **2012**, 37, 181-199.
- 775 Zhang X., Spiers C.J. Compaction of granular calcite by pressure solution at room temperature  
776 and effects of pore fluid chemistry. *International Journal of Rock Mechanics and Mining  
777 Sciences*, **2005**, 42/7-8, 950-960.
- 778
- 779